








Please cite the Published Version

Hymas, Kieran , Soncini, Alessandro , Vignesh, Kuduva R , Chauhan, Deepanshu, Swain, Abinash, Benjamin, Sophie L , Borah, Dipanti, Shanmugam, Maheswaran, Wernsdorfer, Wolfgang , Rajaraman, Gopalan, Langley, Stuart K  and Murray, Keith S  (2024) Discriminating ferrotoroidic from antiferrotoroidic ground states using a 3d quantum spin sensor. npj Quantum Materials, 9 (1). 106 ISSN 2397-4648

DOI: <https://doi.org/10.1038/s41535-024-00712-9>

Publisher: Springer

Version: Published Version

Downloaded from: <https://e-space.mmu.ac.uk/637794/>

Usage rights:  Creative Commons: Attribution-Noncommercial-No Derivative Works 4.0

Additional Information: This is an open access article which first appeared in npj Quantum Materials

Data Access Statement: The X-ray crystallographic coordinates for the structure reported in this study have been deposited at the Cambridge Crystallographic Data Centre (CCDC), under deposition number 2106845. These data can be obtained free of charge from the Cambridge Crystallographic Data Centre via www.ccdc.cam.ac.uk/data_request/cif. The Mathematica notebooks used for the implementation of the theoretical models of spin dynamics and electron paramagnetic resonance are available from the corresponding authors upon reasonable request.

Enquiries:

If you have questions about this document, contact openresearch@mmu.ac.uk. Please include the URL of the record in e-space. If you believe that your, or a third party's rights have been compromised through this document please see our Take Down policy (available from <https://www.mmu.ac.uk/library/using-the-library/policies-and-guidelines>)

<https://doi.org/10.1038/s41535-024-00712-9>

Discriminating ferrotoroidic from antiferrotoroidic ground states using a 3d quantum spin sensor

Check for updates

Kieran Hymas¹✉, Alessandro Soncini²✉, Kuduva R. Vignesh³, Deepanshu Chauhan⁴, Abinash Swain⁴, Sophie L. Benjamin⁵, Dipanti Borah⁴, Maheswaran Shanmugam⁴, Wolfgang Wernsdorfer⁶, Gopalan Rajaraman⁴✉, Stuart K. Langley⁷✉ & Keith S. Murray⁸✉

Molecular toroidal states have come to the forefront as candidates for next-generation quantum information devices owing to their bistability and protection from weak, short-range magnetic interactions. The protection offered by these non-magnetic vortex spin states proves to be a double-edged sword as inferring their existence in a molecular system has yet to be achieved through experimental means alone. Here, we investigate the anomalous, sickle-shaped, single-crystal magnetisation profile arising in μ -SQUID measurements of a novel CrDy_3 molecule. Theoretical modelling supported by ab initio calculations demonstrates that the weak field CrDy_3 spin dynamics is resultant from quantum superposition of the Cr^{III} spin states determined by three competing interactions: (i) the alignment of the Cr^{III} magnetic moment to the external magnetic field, (ii) the zero-field splitting of the Cr^{III} ground quartet, and (iii) coupling to the remnant magnetisation of the toroidal ground state in the Dy_3 triangle. If zero-field splitting of the central transition metal ion is quenched, it operates as a quantum spin sensor, which can be exploited to experimentally discriminate between ferrotoroidic and antiferrotoroidic ground states in MDy_6 double triangle complexes through electron paramagnetic resonance experiments and single-crystal magnetisation measurements with a restricted field sweeping domain.

Since their discovery^{1–5}, single-molecule toroids (SMTs) have garnered significant attention from the molecular magnetism community owing to their rich physics^{6–11}, novel geometries^{12–14} and potential applicability to future quantum information technologies^{15,16}. In addition, the preparation and control of molecular toroidal moments in molecules grafted to spintronic circuits^{17–19} or in STM set-ups²⁰ has been suggested theoretically.

Presently, probing molecular toroidal states through standard experimental means is difficult since their vanishingly small net magnetic moment interacts extremely weakly with external uniform magnetic fields. Alternatively, these moments ought to interact strongly with the curl of a magnetic field $\nabla \times \mathbf{B}$ ^{21,22}, though generating field inhomogeneities on the molecular scale is particularly challenging. Consequently, the existence of ground state toroidal moments in molecular ring systems

must be inferred from experiment through computational and theoretical modelling.

Quantum spin sensors may instead offer a way to detect the minuscule magnetic fields^{23–25} associated with the imperfect cancellation (i.e. broken symmetry) of dysprosium magnetic moments in a toroidal configuration. Nitrogen-vacancy (NV) centres in diamond are typically employed in this vein^{26,27} though, to the best of our knowledge, a successful coupling between the remnant magnetisation of a molecular toroidal moment and a single NV centre, i.e. deposition of a Dy_3 moiety on a diamond surface, has yet to be demonstrated. Trapped ions, neutral alkali atoms and Rydberg atoms mounted in vapour cells have also been suggested as room temperature, electromagnetic field sensors^{28,29}. Accurate field sensing in these set-ups is again dependent upon close proximity of the sensor and analyte³⁰ so how to

¹Commonwealth Scientific and Industrial Research Organisation (CSIRO), Clayton, VIC, Australia. ²Department of Chemical Sciences, University of Padova, Padova, Italy. ³Department of Chemical Sciences, Indian Institute of Science Education and Research (IISER) Mohali, SAS Nagar, Punjab, India. ⁴Department of Chemistry, Indian Institute of Technology Bombay, Mumbai, India. ⁵School of Science and Technology, Nottingham Trent University, Nottingham, UK. ⁶Institute of Quantum Materials and Technologies, Karlsruhe Institute of Technologies, Eggenstein-Leopoldshafen, Germany. ⁷Department of Natural Sciences, Chemistry, Manchester Metropolitan University, Manchester, UK. ⁸School of Chemistry, Monash University, Clayton, VIC, Australia. ✉e-mail: kieran.hymas@csiro.au; alessandro.soncini@unipd.it; rajaraman@chem.iitb.ac.in; s.langlely@mmu.ac.uk; keith.murray@monash.edu

establish an effective coupling through proper spatial localisation of the sensor and the SMT remains an open question. The development of molecular qubits that are grafted or placed in proximity to an analyte is another particularly exciting and promising approach to innocently probe weak intermolecular fields via optical or electrical readout of the perturbed energy gaps in the sensor^{31,32}. What makes them particularly attractive for sensing is a customised, bottom-up synthetic approach that targets specific analytes individually³³. While certainly the most promising candidates for next-generation quantum sensing of molecular properties, the synthesis of a molecular qubit sensor for toroidal ground state configurations has, to the best of our knowledge, not been realised to date.

Chemically grafting a transition metal ion to a molecule containing Dy₃ triangular moieties may offer an experimentally feasible handle to probe for molecular toroidal moments and for the nature of intramolecular toroidal coupling between Dy₃ subunits. Various coupling schemes between transition metal ions and Ln₃ molecular triangles have already been realised in the literature, often in a bid to implement ferrotoroidic (FT) (con-rotating) or antiferrotoroidic (AFT) (counter-rotating) coupling of two distinct toroidal triangles, both to fine tune the extent of ground state toroidicity and to develop materials that display toroidically ordered phases in the quest for novel ferroic or multiferroic properties^{34–42}. Recently, particularly strong experimental evidence was presented for a ferrotoroidically ordered phase in the *quasi*-1D ternary compound Ba₆Cr₂S₁₀⁴³ at around 10 K. Detailed X-ray diffraction and scanning transmission electron microscopy experiments demonstrated unequivocally that the material was composed of 1D chains of dimerised Cr^{III} ions. Magnetic susceptibility and powder neutron scattering experiments revealed an antiferromagnetic coupling between Cr-Cr dimers resulting in a toroidal moment perpendicular to the axis of the spins. While non-collinear magnetic patterns are well known to exist in extended solid state compounds, typically arising as broken symmetry thermodynamic phases below some critical temperature, in molecules, toroidal spin textures are achieved as quantum states of collections of magnetically anisotropic atoms, typically lanthanide ions. In MLn₆ compounds^{37–39}, FT coupling between toroidal quantum states in each Dy₃ triangular moiety has been observed, which may manifest as a ferrotoroidically ordered phase in the crystal, of course below a much smaller temperature $T \sim 0.5$ K. Notably, the sub-Kelvin single-crystal dynamical magnetisation experiments carried out on these molecules always employed magnetic field sweeping domains that were large enough to activate spin-flipped states on single Ln ions, leading to large variations in the molecule's magnetic moment and hence to large steps in the magnetic profile, thus obscuring the detailed magnetic response originating from the central transition metal ion exchange coupled to the toroidal moment.

Here, we describe the synthesis and magnetic characterisation of a novel [Cr^{III}Dy₃^{III}(OH)₄(iso)₆(H₂O)₆]Cl₂ · 5H₂O (iso = isonicotinate) complex (**1**) (denoted CrDy₃ in the following text); a building block towards the previously reported CrDy₆ double triangle³⁷. In addition to the prediction of a CrDy₃ ground state toroidal configuration, we explain the atypical sickle-shaped magnetisation curve stemming from our μ -SQUID measurements using a dynamical master equation model that accounts for the coupled spin dynamics of the Dy₃ triangle and the Cr^{III} magnetic moment. Consequently, we demonstrate that a transition metal ion grafted to a Ln₃ triangle can act as an intramolecular quantum spin sensor, sensitive to the symmetry-breaking properties of the surrounding environment by virtue of weak intramolecular interactions and propose a mechanism for the experimental discrimination between FT and AFT ground states in 3d-4f heterometallic MDy₆ double triangle complexes.

Results

Synthesis and magnetic properties of CrDy₃

Complex **1** is formed from the reaction of CrCl₃ · 6H₂O, Dy(NO₃)₃ · 6H₂O, with isonicotinic acid in the presence of triethylamine. X-ray single crystals are grown from MeOH/Et₂O to yield purple crystals, which were analysed using single crystal X-ray diffraction techniques to allow for structural

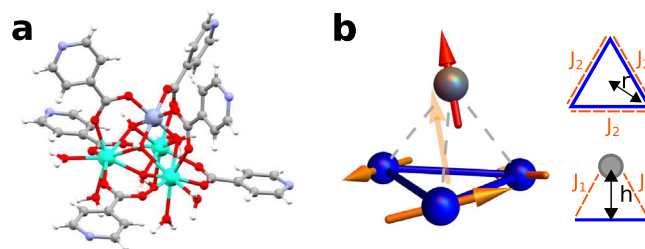


Fig. 1 | Structure of CrDy₃. **a** Crystal structure of **1** where Dy ions are shown in cyan, Cr in purple, O in red, N in blue, C in grey and H in white. **b** Stylised depiction of paramagnetic centres in CrDy₃ with solid orange arrows showing the ab initio computed Dy^{III} magnetic moments in one of the ground state vortex configurations. The translucent orange arrow indicates the direction of a remnant magnetic moment from the imperfect cancellation of the Dy^{III} moments which couples anti-ferromagnetically to the $S = \frac{3}{2}$ Cr^{III} spin shown in red. A schematic of the complex is shown on the right highlighting the circumscribed radius r , and the height of the complex h as well as the exchange coupling J_1 between the transition metal ion and Dy^{III} cations in the triangle, and the intratriangle dysprosium exchange coupling J_2 .

elucidation. Complex **1** crystallizes in the orthorhombic space group, Pnma. Complex **1** is a tetranuclear complex consisting of three Dy^{III} ions and a Cr^{III} ion (Fig. 1a). The metallic core can be described as a {Dy₃Cr(OH)₄} distorted cubane structure with the metal ions and four OH⁻ ions at the vertices of the cube. Alternatively, it can be viewed as a {Dy₃^{III}} triangle lying above a 'central' metal ion site i.e. the building block towards the previously reported CrDy₆ double triangle complex³⁷. The metallic core is stabilised by four hydroxide ions, six isonicotinate and six water ligands. Each hydroxide ion displays a μ_3 bonding mode. Three of the hydroxide ligands connect the Cr^{III} ion to two Dy^{III} ions within a triangle, while the fourth connects the three Dy^{III} ions within the triangle. Three of the isonicotinate ligands bridge (μ_2) between two Dy^{III} ions, while three bridge (μ_2) between a Dy^{III} and Cr^{III} ion. Two water molecules are terminally bound to each Dy^{III} ion. The Cr^{III} ion is six coordinate with an octahedral geometry and a Cr^{III}O₆ environment. The average Cr^{III}O₆ bond length is 1.977 Å. Each Dy^{III} ion is eight-coordinate with a triangular dodecahedron geometry. The average Dy-O bond length is found to be 2.38 Å.

The dynamical magnetisation measurements reported in Fig. 2 show qualitatively different magnetisation profiles for single-crystals of CrDy₃ and of the previously reported³⁷ CrDy₆ complex at a broad range of sweeping field rates using the μ -SQUID technique⁴⁴. In contrast to the stepped hysteresis with a central plateau reported below for CrDy₆ (as well as for the prototypical Dy₃ SMT¹ and several other MDy₆ complexes³⁹), the dynamical magnetisation of CrDy₃ appears as an upright, sickle-shaped magnetisation curve with hysteresis loops emerging only sparingly at $B \sim \pm 50$ mT suggesting a molecular spin relaxation time much faster than the timescale of the sweeping field. In addition, the very tight hysteresis loops either side of $B = 0$ T are completely quenched at zero magnetic field despite the broad range of sweeping speeds explored.

The origin of the stepped magnetisation profiles for CrDy₆ and Dy₃ have recently been discussed^{2,4,37} and attributed to transitions between toroidal and strongly magnetic states associated with multiple flips of dysprosium magnetic moments within the triangular subunits. The slow-relaxation, and hence emergence of magnetic hysteresis in CrDy₆, was then attributed to lagging of population transfer between Dy-flipped states which occurred at a rate slower than the time evolution of the tracing magnetic field. If the same mechanism exists for CrDy₃, a lack of both hysteresis loops and discrete steps in the dynamical magnetisation is suggestive of a rather different low energy Hilbert space, a stronger interaction with the dissipative environment of the crystal or a mixture of both. Alternatively, the magnetic response measured by the μ -SQUID could originate from the fast-fluctuating Cr^{III} ion which is perturbed by the Dy^{III} ions in the triangular subunit. We will disentangle these two possible mechanisms in the following section.

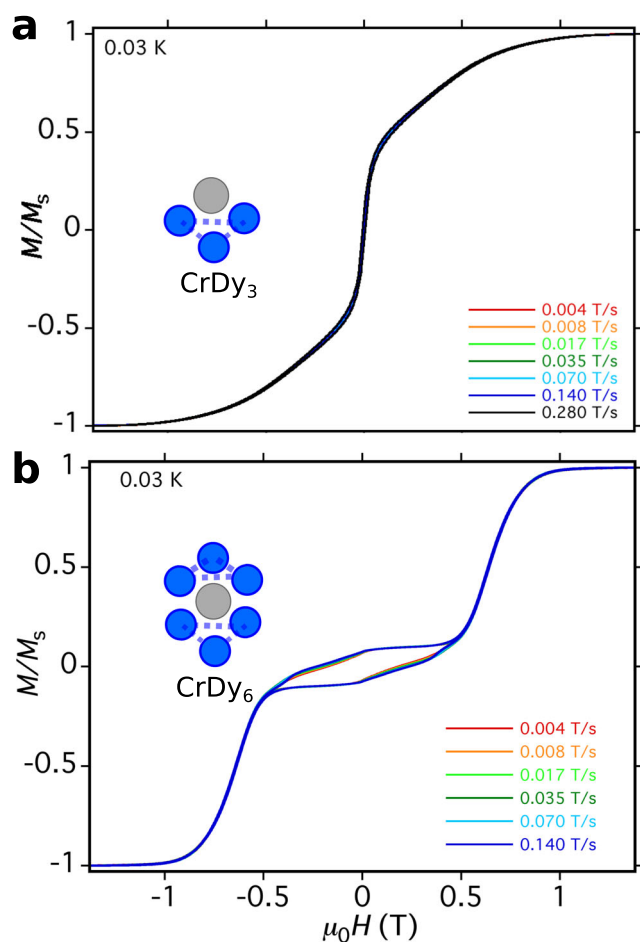


Fig. 2 | Single-crystal magnetisation comparison. **a** Single-crystal magnetisation vs. field plot of complex **1** CrDy₃ at $T = 0.03$ K for a variety of field tracing rates. **b** Single-crystal magnetisation of a related complex CrDy₆ previously reported³⁷. Note the lack of magnetic hysteresis in the former complex despite a faster field sweep rate than in the latter.

Theoretical modelling of the sickle-shaped magnetisation

To understand the striking qualitative difference between the single-crystal magnetisation profile of CrDy₆ and its symmetry reduced analogue CrDy₃, we first performed scalar-relativistic multi-configurational ab initio calculations to determine the electronic structure of the isolated paramagnetic ions within the CrDy₃ molecule using the MOLCAS 8.0 suite⁴⁵. For each of the Dy^{III} centres, CASSCF+RASSI-SO calculations followed by an M_J decomposition of the resultant wavefunctions revealed energetically well-isolated (by ~ 130 cm⁻¹), almost pure $|M_J = \pm 15/2\rangle$ Kramer's ground doublets with axial g-tensors arranged around the vertices of the triangle. In particular, the g-tensor main values for each of the dysprosium ions were (Dy1: $g_x = 0.012$, $g_y = 0.025$, $g_z = 19.56$), (Dy2: $g_x = 0.014$, $g_y = 0.021$, $g_z = 19.47$), (Dy3: $g_x = 0.045$, $g_y = 0.058$, $g_z = 19.38$). The ab initio computed magnetic anisotropy axes of the dysprosium ions are shown in Fig. 1b where an alternating out-of-plane canting angle underscores the departure from a perfect tangential arrangement of the Dy^{III} magnetic moments. As a consequence of their strongly axial g-tensors, to a good approximation the p^{th} Dy^{III} ion may be considered as a semi-classical Ising spin oriented along its ab initio principal magnetic axis with its orientation labelled by the quantum number $m_p = \pm 1$. The configuration of the Dy₃ moiety is thus labelled by the vector $\mathbf{m} = (m_1, m_2, m_3)$.

Ab initio computed Loprop and Mulliken charges for **1** are shown in Fig. 3. Considering both cases, the largest computed charges are observed on the four μ_3 -O atoms of the hydroxide ligands which constitute the CrDy₃ core motif. As the ground state of the Dy^{III} ion has oblate electron density,

the β electron density usually lies perpendicular to the direction where large electrostatic repulsion is found. Thus in each of the Dy^{III} ions, the main magnetic anisotropy axes (g_{zz}) lie parallel to atoms possessing the largest charges, causing the g_{zz} axes to adopt the approximately tangential configuration about the vertices of the triangle. In addition, the 'larger' charges found on the μ_3 -O of the hydroxide ligand, in comparison to the O atoms of isonicotinic acid and H₂O ligands, influence the crystal field splitting, contributing to the rather large separation of ground and first excited state (~ 130 cm⁻¹) in each Dy^{III} ion. To ascertain whether the orientation of the H₂O ligands affected the magnetic anisotropy of Dy^{III}, we performed additional CASSCF calculations on CrDy₃ with the coordinating water molecules in different orientations (see Supplementary Fig. 1 and Supplementary Tables 4–7). All orientations lead to strongly axial g-tensors and similar ground to first excited state gaps ≥ 120 cm⁻¹ other than when the symmetry plane containing both O-H bonds of the water molecule was parallel to the isonicotinate ring. In that case, sizeable magnetic anisotropy was still observed however with a reduced first excited state gap ~ 80 cm⁻¹ on one of the Dy^{III} ions. The presence of the Cr^{III} ion and its partial polarisation on the attached charges, relatively smaller than on μ_3 -O, leads to the alignment of the g_{zz} axis of Dy^{III} roughly in the plane of the Dy₃ motif.

Similar CASSCF+RASSI-SO calculations were performed for the central Cr^{III} ion yielding a ground state spin quartet $S = 3/2$ with an isotropic g tensor (Cr: $g_x = g_y = g_z = 1.96$). Remarkably, our ab initio calculations predict a zero-field splitting of the Cr^{III} ground spin manifold ~ 0.5 cm⁻¹, along a magnetic axis approximately perpendicular to the triangular plane. This splitting is three orders of magnitude larger than what was previously predicted for the central Cr^{III} ion in the higher symmetry CrDy₆(NO₃) complex³⁷ and an order of magnitude larger than predicted for CrDy₆(Cl)³⁹.

To arrive at an effective model for the low-lying electronic structure for CrDy₃ and its magnetic response, we appropriately adapt the established theoretical framework used to study CrDy₆ and other MDy₆ clusters^{37,39} to account for a single Dy₃ triangle only. We thus account for intramolecular exchange interactions as well as magnetic dipole-dipole coupling between all paramagnetic centres in the CrDy₃ molecule with the Hamiltonian $H_{\text{mol}} = H_{\text{ex}} + H_{\text{dip}} + H_{\text{zfs}}$ (details reported in the 'Methods' section) projected onto the basis of the lowest lying Kramer's doublets of each of the Dy^{III} ions and the $|M_{\text{Cr}}\rangle$ spin states of the Cr^{III} ground quartet. Using the average interatomic Dy-Dy and Cr-Dy distances, $r = 2.19$ Å and $h = 2.57$ Å as well as the ab initio computed magnetic axes, our effective model predicts a ground state toroidal configuration $\pm \tau = (\pm 1, \pm 1, \pm 1)$ of the Dy^{III} magnetic moments. Owing to the imperfect cancellation of the Dy^{III} magnetic moments (see Fig. 1b), a remnant magnetisation almost perpendicular to the plane of the Dy₃ triangle results from the ground state toroidal configuration. The magnitude of the remnant magnetisation M_{rem} , is equivalent to that which would arise from a perfectly tangential arrangement of the Dy^{III} magnetic moments about the vertices of the triangle with an average out-of-plane canting angle $\eta \approx 1^\circ$.

In Fig. 4a and b we show the experimental isothermal magnetisation at $T = 2, 3, 4$ and 5 K and the magnetic susceptibility (dots) and compare the resultant curves to simulations of the same quantities from our theoretical model (solid lines) with $J_1 = -0.4$ cm⁻¹ and $J_2 = -0.01$ cm⁻¹ as the only fitting parameters of our model. The theoretical curves agree particularly well with the experiments despite underestimating the experimental magnetisation at high fields (a symptom of magnetic torquing in the experiment). Despite the absence of a characteristic S-shaped powder magnetisation curve (which typically indicates a non-magnetic ground state in SMTs), the tendency of our magnetic susceptibility measurements towards $\chi_m T \rightarrow 0$ as $T \rightarrow 0$ provides evidence of a weakly magnetic CrDy₃ ground state in agreement with our theoretical predictions (see the low energy Zeeman diagram of CrDy₃ in Fig. 4c). Notably, the exchange coupling constants predicted by density functional theory (DFT) calculations on CrDy₃ did not lead to a good reproduction of the experimental magnetic measurements. The failure of DFT to extract meaningful exchange coupling constants in this case may point towards a subtlety in the electronic structure of CrDy₃ that warrants further investigation. Lastly, in Fig. 4d we compare

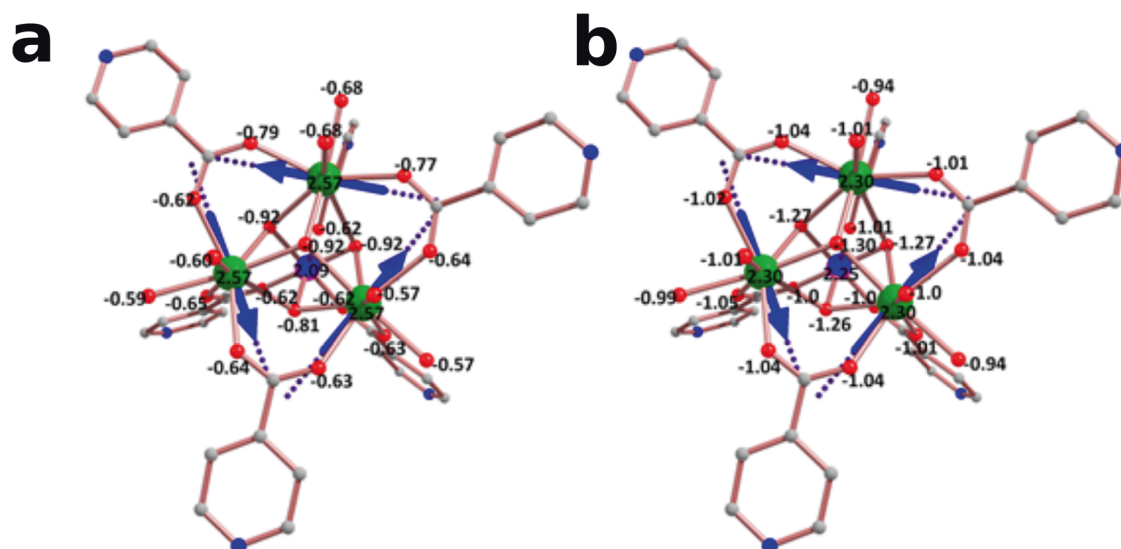


Fig. 3 | Ab initio charge density analysis of CrDy_3 . Ab initio computed **a** Loprop and **b** Mulliken charges on the donor atoms of complex **1**.

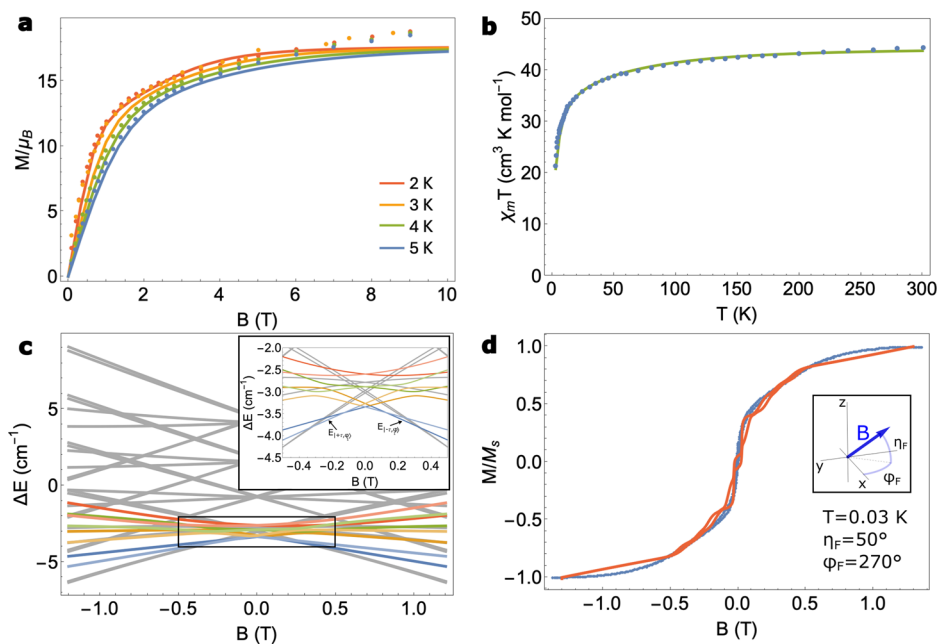


Fig. 4 | Experimental and theoretical simulations of CrDy_3 magnetic properties. **a** Comparison of the experimental isothermal powder magnetisation (dots) with the simulated powder magnetisation (solid lines) at $T = 2, 3, 4$ and 5 K. **b** Comparison of the experimental zero-field powder magnetic susceptibility versus temperature (blue dots) with the simulated $\chi_m T$ (green solid line). **c** Zeeman energy levels of the thirty-two dimensional Hilbert space of CrDy_3 using $J_1 = -0.4 \text{ cm}^{-1}$ and $J_2 = -0.01 \text{ cm}^{-1}$ obtained from fitting to (a, b). The coloured lines correspond to Zeeman energies of states with a vortex configuration of the Dy^{III} magnetic moments (the lighter (darker) colour represents a clockwise (anticlockwise) vortex configuration). The applied field is chosen almost exactly along the intrinsic magnetic

anisotropy axis of the Cr^{III} ion which was obtained from ab initio calculations. The inset shows a zoomed-in picture of the boxed region where, at zero-field the system exhibits a doubly degenerate ground state toroidal moment in the wheel. **d** Comparison between the experimental single-crystal magnetisation at $T = 0.03$ K (blue dots) and our theoretical simulations of the single-crystal magnetisation from a master equation model (red solid line). For the simulations we found the best agreement with experiment when the field was oriented roughly along the magnetic anisotropy axis of the Cr^{III} ion. We employed a spin-phonon coupling constant $\Gamma = 5 \times 10^4 \text{ cm}^3 \text{ s}^{-1}$, a quantum tunnelling matrix element $\gamma/h = 10^6 \text{ s}^{-1}$, a Lorentzian broadening factor $\lambda = 10^{10} \text{ s}^{-1}$ and a field sweep rate $\omega = 0.28 \text{ T s}^{-1}$.

the experimental single-crystal magnetisation with our simulated magnetisation obtained from numerical integration of an adiabatic master equation. In our master equation we account for a modified spin dynamics of the CrDy_3 in the presence of an oscillating applied magnetic field owing to dissipative interactions with the crystal environment e.g. spin-phonon mediated magnetic relaxation and stray-field induced quantum tunnelling mechanisms^{37,39}. We find rather good agreement between the sickle-shaped

experimental magnetisation and our theoretical prediction when the dynamically sweeping magnetic field is oriented approximately along the magnetic anisotropy axis of the Cr^{III} spin.

To understand the sickle-shaped magnetisation curve, we plot the time-evolution of the relevant state populations for a forward sweep of the field in Supplementary Fig. 2. At large, negative values of the applied field, magnetic states of the Dy_3 wheel are activated with dominant contributions

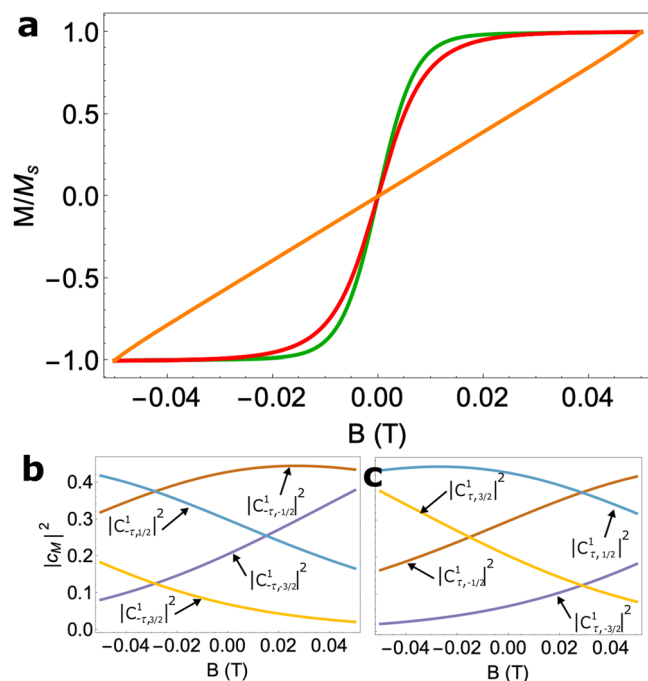


Fig. 5 | Toroidal state sensing in CrDy₃ in the weak field limit. **a** Simulated quasi-static magnetisation in the case of a free-fluctuating spin $\frac{3}{2}$ i.e. a Brillouin function (red curve), the CrDy₃ molecule explored in the main text (green curve) and CrDy₃ without Cr^{III} zero-field splitting (orange curve). The squared amplitudes of the ground state Cr^{III} wavefunctions with **b** clockwise and **c** anticlockwise toroidal configuration in the Dy₃ moiety, when Cr^{III} zero-field splitting is quenched in the restricted field sweeping regime $-50 \text{ mT} \leq B \leq 50 \text{ mT}$.

to the single-crystal magnetisation. It is worth noting that, since these states have a large magnetic moment only in the plane of the Dy₃ triangle and the field is applied almost perpendicularly (along the Cr^{III} magnetic anisotropy axis), the resultant cosine contributing to the magnetisation is comparable to the spin of the Cr^{III} ion. Interestingly, even at $B = 1 \text{ T}$ the antiferromagnetic interaction between the Cr^{III} spin and the magnetic states in the Dy₃ wheel overcomes the energy for realignment of the Cr^{III} spin to the applied field. As the field is swept forward, a level crossing with one of the toroidal states is reached and a fast quantum tunnelling of the magnetisation transitions the system into a pure toroidal configuration where, for weak fields, the magnetic response is dominated by the Cr^{III} spin only. The time reversed situation occurs once the system passes through zero field and a further quantum tunnelling event transitions the Dy₃ wheel back to a magnetic configuration.

Close inspection of the Cr^{III} wavefunction amplitudes in the restricted sweeping domain where only the toroidal configurations are populated, reveal somewhat mixed Cr^{III} wavefunctions as a result of competing interactions between alignment against the intrinsic magnetic anisotropy axis of Cr^{III}, the weak remnant magnetisation of the Dy₃ wheel and the weak applied field. This mixing is a signature of the Cr³⁺ spin sensing mechanism and results in a deviation of the single-crystal magnetisation from what might be expected of a free-fluctuating Cr^{III} spin that instantaneously responds to an applied field (see the red and green curves in Fig. 5a). This deviation is even more prominent when the intrinsic magnetic anisotropy of the Cr^{III} ion is quenched (orange curve in Fig. 5a) leading to a much stronger mixing of the Cr^{III} spin states in this restricted field sweeping region (Fig. 5b, c) and thus represents a definitive experimental-only measure of the toroidal states in Dy₃. In fact, in Supplementary Note 1, we also explore the situation wherein the sickle-shaped magnetisation of CrDy₃ can be entirely explained by the response of the Cr^{III} alone, influenced only by its intrinsic magnetic anisotropy and coupling to the remnant magnetic field of the toroidal states. The powder

magnetisation measurements made on CrDy₃ (Fig. 4a) did not support this hypothesis, however. In either case, the zero-field splitting in Cr^{III} cannot be easily disentangled from the exchange anisotropy introduced by the remnant magnetic moment of the toroidal states. In the next section we will illustrate how the combination of (i) quenching transition metal sensor zero-field splitting and (ii) restricting the sweeping domain of the ac field, leads to a clear FT/AFT discrimination in MDy₆ compounds.

Sensing ferrotoroidic or antiferrotoroidic ground states in MDy₆ complexes

Taking inspiration from the CrDy₃ model system, we turn our attention to the detection of FT or AFT ground states in the MDy₆ parent complexes^{37,39}. Recently, the intimate correlation between the structure and ground state magnetic properties of MDy₆ complexes was exposed systematically by varying the central 3d transition metal ion M^{III} and the counter anion (Cl⁻ or NO₃⁻) across each complex³⁹. Importantly, the assignment of a FT or AFT ground state Dy configuration for each complex was made possible only via theoretical models which were used to simulate magnetisation and susceptibility experiments. In the case of M^{III} = Cr^{III}, a FT ground state was predicted³⁷ that was characterised by con-rotating vortex arrangements of the Dy^{III} magnetic moments in each triangular subunit. These magnetic moments cancel exactly owing to the inversion symmetry of the molecule resulting in a net zero remnant magnetic moment from the Dy₃-Dy₃ motifs. On the other hand, for M^{III} = Fe^{III}, the ground state was predicted to be AFT³⁹ thus leading to a remnant out-of-plane magnetic moment as a result of the counter-rotating vortex arrangements of Dy^{III} moments in each triangle.

While single-crystal magnetisation measurements of these complexes were made in the aforementioned study, the sweeping domain was chosen so that dynamical transitions to strongly magnetic, Dy-flipped configurations of the Dy^{III} moments dominated the magnetic hysteresis measurements thus obscuring the fine details of the central 3d metal ion spin dynamics. If the same measurements were made but with the sweeping range restricted only to activate states from either the ground FT or AFT configurations, then the observation of a free fluctuating central metal ion spin (Brillouin magnetisation curve) or one coupled to a remnant magnetisation (sickle-shaped magnetisation curve) would be diagnostic of a FT or AFT ground state configuration, respectively. This would of course assume no intrinsic magnetic anisotropy (i.e. zero-field splitting) of the central metal ion spin levels. Such a situation may be realised by the substitution of $S = \frac{1}{2}$ Cu^{II} for the central metal ion of MDy₆; automatically quenching zero-field splitting effects.

Using an effective theoretical model akin to that presented above, we set-out to prove this effect for a CuDy₆ complex. We describe the magnetic axes of the p^{th} dysprosium ion in each complex as $\mu_p = (-\sin(\theta_p - \phi) \cos(\eta), \cos(\theta_p - \phi) \cos(\eta), \pm \sin(\eta))$ where $\theta_p \in \{0, \frac{2\pi}{3}, \frac{4\pi}{3}, -\frac{\pi}{3}, \pi, \frac{\pi}{3}\}$, η and ϕ are the average angles of distortion away from a perfect tangential arrangement of the Dy moments around each triangular unit and \pm corresponds to a Dy^{III} ion in the upper and lower triangular plane of each molecule. For the purposes of illustration, we utilise in our calculation the average geometric quantities r , h , η , ϕ and the DFT computed exchange coupling J_2 obtained for CrDy₆(NO₃) now with Cr^{III} replaced with Cu^{II}. Accounting for the intramolecular exchange coupling and dipolar interactions, we compute the single-crystal magnetisation for $J_1 = -0.1 \text{ cm}^{-1}$ (resulting in a FT ground state) and $J_1 = -1 \text{ cm}^{-1}$ (resulting in an AFT ground state) in a field domain restricted to only thermally populate the FT and AFT ground manifolds of each complex.

In Fig. 6b we present simulations of single-crystal magnetisation for CuDy₆ with FT and AFT Dy₃-Dy₃ ground configurations. At $T = 0.01 \text{ K}$ (a temperature accessible to μ -SQUID magnetometers) there is only enough thermal energy to populate the ground FT or AFT manifolds of each molecule; the two manifolds being separated in energy from a combination of intertriangle dipolar interactions and exchange coupling to the central metal ion. When a field is applied $\eta_F = 10^\circ$ out of the plane of the triangular

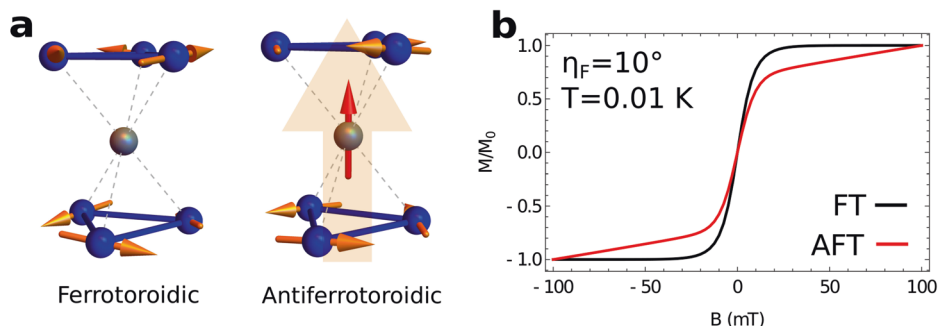


Fig. 6 | Discriminating between ferrotoroidic and antiferrotoroidic ground states. **a** Schematic depiction of the CuDy₆ complex displaying ferrotoroidic (left) and antiferrotoroidic (right) ground state configurations in the absence of a magnetic field. The perfect cancellation of inversion related Dy^{III} magnetic moments in the ferrotoroidic ground state leaves the central Cu^{II} spin free-fluctuating whereas in the antiferrotoroidic case the central metal ion couples to the remnant out-of-plane magnetic moment of the Dy₃ subunits (transparent orange arrow). **b** Simulations of

single crystal magnetisation at T = 0.01 K for CuDy₆ with a ferrotoroidic (black) and antiferrotoroidic (red) ground state, when a field is applied η_F = 10° out of the Dy₃ plane and swept in a domain restricted to probe only the ferrotoroidic/antiferrotoroidic manifolds. While the response of CuDy₆ with a ferrotoroidic ground state to the magnetic field is archetypal of a free-fluctuating S = 1/2, the alignment of the Cu^{II} ion to the field in the antiferrotoroidic ground state is impeded by coupling to the remnant magnetisation of the Dy^{III} moments.

subunits, the FT complex gives the magnetic response typical of a free-fluctuating Cu^{II} ion (i.e. a S = 1/2 Brillouin function) which remains completely insensitive to the field sweeping orientation (see Supplementary Fig. 7). In contrast, the magnetic response of the AFT complex departs from the behaviour of a free-fluctuating spin and a sickle-shaped magnetisation curve is recovered similarly to CrDy₃. Notably, the magnetisation profile of this molecule is particularly sensitive to field orientation (Supplementary Fig. 7). Owing to a summation rather than a cancellation of the out-of-plane Dy₃ magnetic moments in the AFT ground state, a competition emerges between the alignment of the central Cu^{II} spin moment to the remnant magnetic moment of Dy₃-Dy₃ and to the applied field.

Figure 6 b shows that the magnetisation profile of a free-fluctuating spin (associated with a FT ground state) differs significantly from a spin coupled to a remnant magnetisation (associated with an AFT ground state). Observation of these quantitatively different single-crystal magnetisation curves provides a diagnostic test for a FT or an AFT ground state in MDy₆ complexes, without the need for theoretical modelling.

We also predict, in the proposed CuDy₆ complex, that a FT or an AFT ground state can be sensed via spectroscopic methods such as electron paramagnetic resonance (EPR). Here we present powder EPR simulations demonstrating the distinctive lineshapes which occur from each ground state configuration and thus facilitate EPR FT/AFT discrimination. For low enough temperatures and restricted field-sweeping domains, only the FT or AFT ground configurations are thermally populated in the complex. Since EPR transitions between FT and AFT states involve the simultaneous inversion of three Dy^{III} magnetic moments, they can be safely neglected. Thus only transitions between the spin states of the central Cu^{II} S = 1/2, which are Dy₃-Dy₃ configuration preserving, are allowed. The relevant Zeeman energies (and hence Zeeman gaps to be interrogated in the EPR experiment) can be expressed analytically

$$\begin{aligned}
 E_{|\pm\tau, \pm\tau, \pm\rangle} &= \pm \frac{1}{2} g\mu_B |\mathbf{B}| \\
 E_{|+\tau, -\tau, \pm\rangle} &= \Delta_{\text{AFT-FT}}^{\text{dip.inter}} + 6\mu_B \bar{\mu} B_z \sin \eta \\
 &\quad \pm \frac{1}{2} \sqrt{(g\mu_B B_z + \Lambda)^2 + (g\mu_B B_\perp)^2} \\
 E_{|-\tau, +\tau, \pm\rangle} &= \Delta_{\text{AFT-FT}}^{\text{dip.inter}} - 6\mu_B \bar{\mu} B_z \sin \eta \\
 &\quad \pm \frac{1}{2} \sqrt{(g\mu_B B_z - \Lambda)^2 + (g\mu_B B_\perp)^2}
 \end{aligned} \quad (1)$$

where $\Delta_{\text{AFT-FT}}^{\text{dip.inter}} = E_{\text{AFT}}^{\text{dip.inter}} - E_{\text{FT}}^{\text{dip.inter}}$ is the intertriangle magnetic dipole-dipole coupling energy difference between FT and AFT semi-classical Dy^{III} magnetic moment configurations (see Eq. (4)). This contribution depends only on the geometry of the molecule (i.e. the values of r, h, η and φ) and can

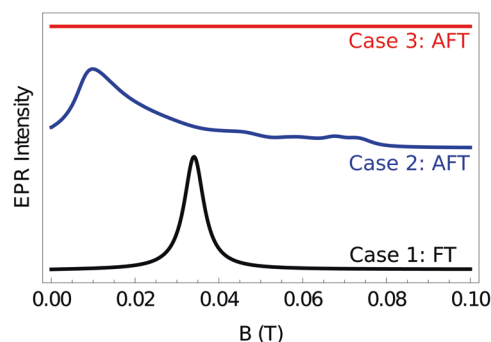


Fig. 7 | Spectroscopic discrimination between ferrotoroidic and antiferrotoroidic ground states. Simulated zero temperature, field-swept, powder electron paramagnetic resonance spectra of CuDy₆ for the three possible ground state configurations described in the main text. Each spectrum is offset for clarity. For a ferrotoroidic ground state (black curve), a strong, narrow signal is observed archetypal of an isotropic S = 1/2. For a molecule with an antiferrotoroidic ground state and only modest 3d – 4f exchange splitting (blue curve), a much broader signal is observed. In case 3 (red curve), the exchange splitting is larger than the available photon energy and as such, no transitions at zero temperature can occur.

stabilise an AFT ground state when the out-of-plane canting angle η is non-negligible (e.g. an AFT configuration is stabilised in the CrDy₆ molecule if η ≳ 10°). The exchange coupling of the Cu^{II} spin to the remnant magnetic moment in the AFT configuration leads to a term $\Lambda = [3\mu_0 \mu_B^2 g \bar{\mu} / (2\pi \sqrt{r^2 + h^2}) - 15J_1] \sin \eta$ in the second and third Zeeman energies reported in Eq. (1). These are sensitive both to the exchange coupling strength J₁ and to the molecular geometry. Note that the ‘±’ on the right hand sides of Eq. (1) refer to the Cu^{II} spin eigenstates for each Dy₃-Dy₃ configuration.

On varying the parameters J₁ and η in Eq. (1), three distinct low energy Zeeman spectra can be generated; these are depicted in Supplementary Fig. 8. For small canting angle η and small Cu-Dy exchange coupling J₁, a FT ground state is observed with AFT doublets as first and second excited states, we refer to this situation as case 1. For larger canting angles the previous situation is reversed and the AFT doublets are both energetically stabilised, this is case 2. Alternatively, if the coupling J₁ between the remnant Dy₃-Dy₃ magnetic moment and the quantum spin is sizeable, then a third scenario is realised where only one of the AFT doublets is stabilised at zero field. For this third case, the FT quartet is the first excited state of the system, and the second excited state is another AFT doublet.

In Fig. 7 we illustrate that each of these cases may be inferred from zero temperature, field-swept powder EPR measurements. For a FT ground

configuration where the remnant magnetic moment of Dy_3 - Dy_3 is zero, a signal appears in the EPR spectrum when the radiation frequency $\nu = g\mu_B|\mathbf{B}|/h$. Clearly this signal is isotropic with respect to field orientation and thus gives rise to a single, tight Lorentzian lineshape in the powder EPR spectrum (case 1: black curve). On the other hand, for an AFT ground configuration, a signal is observed when $\nu = \sqrt{(g\mu_B B_z - \Lambda)^2 + (g\mu_B B_{\perp})^2}/h$. This resonance condition is patently field orientation dependent and thus, as a consequence of powder averaging, results in a spectrum of many overlapping resonances which convolute into a greatly broadened EPR lineshape (case 2: blue curve). If the $3d-4f$ exchange coupling J_1 is so large that the previous resonance condition can not be met in the restricted field sweeping domain, then no signal is observed in the EPR experiment (case 3: red curve). We note finally that these three cases can be further interrogated with variable temperature and variable frequency powder EPR experiments as simulated in Supplementary Fig. 9.

Discussion

We have demonstrated that the weak field region of the sickle-shaped magnetisation profile of $CrDy_3$ results from a linear superposition of Cr^{III} spin states which, in the absence of intrinsic magnetic anisotropy, offer a mechanism to probe the toroidal ground states of the Dy_3 triangle. Owing to the sizeable zero-field splitting of the ground Cr^{III} spin manifold, theoretical modelling is still necessary to untangle the microscopic mechanisms leading to the sickle-shaped magnetisation curve of $CrDy_3$. Measuring the altered magnetic response of an isotropic spin system grafted to a Dy_3 triangle however, offers an experimental-only method to probe the tiny intramolecular magnetic fields associated with imperfect cancellation of Dy^{III} magnetic moments in a toroidal configuration without interfering directly with their stabilisation.

The extent to which zero-field splitting of the central transition metal ion in MDy_6 contributes to the deviation of single-crystal magnetisation measurements from the case of a free-fluctuating isotropic spin, can be addressed experimentally by preparing MDy_6 complexes with a central spin $S = \frac{1}{2}$. In the case of a $3d^9$ Cu^{II} ion, a configuration realised in $CuDy_3$ polymers³⁵, the mechanism exposed above tells us that if the single-crystal magnetisation profile behaves like a $S = \frac{1}{2}$ Brillouin function independent of field orientation, then this signals a FT ground state. If the single-crystal magnetisation appears sickle-shaped and strongly field-orientation dependent, this signals an AFT ground state. In general though, provided that the intramolecular exchange and magnetic dipole-dipole interactions between the central transition metal ion and the remnant magnetic moment of the Dy_3 subunits are larger than zero-field splitting effects in the central transition metal ion, as is the case for $CrDy_6(NO_3)$, the magnetic response of the central metal ion alone can be indicative of the FT/AFT ground state character of the molecule. Spectroscopic methods such as electron paramagnetic resonance which probe the magnetic response of the central quantum spin, also offers a qualitative measurement of the ground state Dy_3 - Dy_3 configuration.

In summary, we have presented the synthesis, structural and magnetic characterisation of a novel $CrDy_3$ molecule exhibiting a ground state toroidal Dy_3 configuration. Theoretical modelling supported by scalar relativistic multi-configurational ab initio calculations demonstrated that the complex's anomalous sickle-shaped magnetisation curve arises from the coupled spin dynamics of the central Cr^{III} ion and the activation of magnetic levels in the Dy_3 wheel at larger fields. The sickle-shape in particular was indicative of a fast dissipative dynamics and the compression of the Zeeman levels caused by sizeable zero-field splitting of the Cr^{III} ground spin quartet and antiferromagnetic coupling of the Cr^{III} spin to a small remnant magnetisation in the Dy_3 triangle. After the quenching of intrinsic zero-field splitting, we suggested that the central transition metal ion of heterometallic MDy_6 complexes may be employed as a quantum spin sensor for ground state FT/AFT discrimination in complementary magnetic and spectroscopic experiments.

Methods

Synthesis of $CrDy_3$

$CrCl_3 \cdot 6H_2O$ (0.016 g, 0.1 mmol) was gently heated in acetonitrile to give a purple solution. $Dy(NO_3)_3 \cdot 6H_2O$ (0.22 g, 0.5 mmol) and isonicotinic acid (0.12 g, 1 mmol) were then added. Triethylamine (0.4 mL, 0.3 mmol) was subsequently added dropwise to reveal a blue/green solution and the reaction was left to stir for 2–3 h at 70 °C. After this time the solvent was removed, and the resulting oil was redissolved in methanol. After layering the methanol with diethyl ether, pale purple/pink single crystals grew within 3–4 days. Anal. Calculated (found) for **1**: $CrDy_3C_{36}H_{50}O_{27}N_6Cl_2$: C, 26.87 (26.67); H, 3.13 (3.19); N 5.22 (5.11).

X-ray crystallography

X-ray single-crystal structural data for **1** were collected on an Agilent Xcalibur diffractometer equipped with a fine-focus sealed tube X-ray source with graphite monochromated Mo- $K\alpha$ radiation. The programme CrysAlis PRO⁴⁶ was used for the data collection, cell refinement and data reduction. Complex **1** was solved by direct methods (SHELXS-97)⁴⁷, and refined (SHELXL-97)⁴⁸ by full least matrix least-squares on all F^2 data. Crystallographic data and refinement parameters for **1** are summarised in Supplementary Table 1.

Magnetic measurements

The temperature-dependent direct current magnetic susceptibility of a polycrystalline sample of $CrDy_3$ was measured from 1.8 to 300 K using an external magnetic field of 5 kOe with a Quantum Design PPMS SQUID magnetometer. At room temperature, $\chi_m T = 44.04$ cm³ K mol⁻¹, in good agreement with the theoretical value of 44.38 cm³ K mol⁻¹ expected for one Cr^{III} ($S = 3/2$, $g = 2$, $C = 1.875$ cm³ K mol⁻¹) and three uncoupled Dy^{III} ions ($J = 15/2$, ${}^6H_{15/2}$, $g = 4/3$, $C = 14.17$ cm³ K mol⁻¹). Field-dependent magnetisation measurements were performed at 2 K within a magnetic field range of 0–9 T.

Magnetisation measurements on a single crystal were performed with an array of μ -SQUIDS for **1**. This magnetometer works in the temperature range of 0.02 to ~7 K and in fields of up to 1.4 T with sweeping rates as high as 10 T s⁻¹, along with a field stability of 1 T. The time resolution is ~1 ms. The field can be applied in any direction of the μ -SQUID plane with precision much better than 0.1° by separately driving three orthogonal coils. In order to ensure good thermalisation, the single crystals were fixed with Apiezon grease.

Computational details

Using MOLCAS 8.0⁴⁵, ab initio calculations were performed on the Dy^{III} ions using the crystal structure of $CrDy_3$ in order to find the anisotropic nature of all Dy centres. While performing the single-ion calculation on each Dy centre, we substituted neighbouring Dy ions with a diamagnetic Lu^{III} ion and a paramagnetic Cr ion with diamagnetic Sc^{III} ion. Relativistic effects are taken into account by employing the Douglas-Kroll-Hess Hamiltonian⁴⁹. The spin-free eigenstates are achieved by the Complete Active Space Self-Consistent Field (CASSCF) method⁵⁰. The basis sets were taken from the ANO-RCC library for the calculations. We have employed the [ANO-RCC...8s7p5d3f2g1h.] basis set for Dy atoms, the [ANO-RCC...6s5p3d2f1g.] basis set for the Cr atom, the [ANO-RCC...3s2p.] basis set for C atoms, the [ANO-RCC...2s.] basis set for H atoms, the [ANO-RCC...3s2p1d.] basis set for N and O atoms, the [ANO-RCC...4s3p2d.] basis set for the Sc atom and the [ANO-RCC...7s6p4d2f.] basis set for Lu^{III} . In the first step, we run a guessorb calculation using Seward module to create the starting guess orbitals. Here, we included nine electrons across seven 4f orbitals of the Dy^{III} ion. Then using these guess orbitals, we have chosen the active space based on the number of active electrons in the number of active orbitals and carried out the SA-CASSCF calculations. Here, the Configuration Interaction (CI) procedure were computed for Dy^{III} ion and considered twenty-one sextet excited states in the calculations to compute the magnetic anisotropy. All the excited states corresponding to the sextet state have been computed in the CASSCF module to calculate the spin-orbit

coupled states. Moreover, these computed SO states have been considered in the SINGLE_ANISO⁵² programme to compute the g-tensors. The g-tensors for the Kramers doublets of Dy^{III} were computed based on the pseudospin $S = \frac{1}{2}$ formalism⁵².

Additionally, the ab initio CASSCF calculations were performed to calculate the g-tensor for Cr^{III} in complex **1**. Here, the active space for CASSCF calculations comprises five Cr^{III}-based orbitals with three electrons in them (*d³* system; CAS(3,5) setup). We considered 10 quartet excited states and 40 doublet excited states for Cr^{III} ion⁵².

Along with Mulliken charges, we also used the Loprop charges to analyse and understand the direction of magnetic anisotropy, which can be computed like a charge, a component of the dipole moment or an exchange-hole dipole moment, is localised by transforming the property of two centres⁵³.

DFT calculations were performed using the B3LYP functional⁵⁴ implemented in the Gaussian 09 quantum chemistry suite⁵⁵. The dysprosium ions in CrDy₃ were replaced with spin-only Gd^{III} ions. We used the double zeta quality Cundari-Stevens effective core potentials for the Gd atoms and the TZV basis set for all others. We performed a series of single point energy calculations, first converging to the high spin state of CrGd₃ and then to broken symmetry states associated with the complete inversion of α to β spin density in valence orbitals localised on the paramagnetic centres. With reference to the Heisenberg-Dirac-van Vleck Hamiltonian, we generate a system of linear equations for the exchange couplings in terms of the high spin and broken symmetry single point energies which, upon rescaling the solutions by S_{Dy}/S_{Gd} and $(S_{Dy}/S_{Gd})^2$ respectively, yields the values $J_1 = 0.3 \text{ cm}^{-1}$ and $J_2 = -0.1 \text{ cm}^{-1}$.

Theoretical model

To model the interactions between the paramagnetic ions in CrDy₃ and thus simulate its magnetic properties, we account for intramolecular exchange interactions as well as magnetic dipole-dipole coupling between the paramagnetic centres in the molecule, the zero-field splitting of the Cr^{III} ion and a coupling to an external magnetic field with the Hamiltonian

$$H = H_{\text{ex}} + H_{\text{dip}} + H_{\text{zfs}} + H_{\text{Zee}}. \quad (2)$$

This Hamiltonian is projected onto the basis of the lowest lying Kramer's doublets of each of the Dy^{III} ions and the $|M_{\text{Cr}}\rangle$ spin states of the Cr^{III} ground quartet leading to a 32-dimensional Hilbert space of states $|\mathbf{m}, M_{\text{Cr}}\rangle \doteq |m_1, m_2, m_3, M_{\text{Cr}}\rangle$. We choose a quantisation axis for the Cr^{III} ion collinear to the applied magnetic field.

The exchange coupling Hamiltonian reads

$$H_{\text{ex}} = -J_1 \sum_p \mathbf{S}_p \cdot \mathbf{S}_{\text{Cr}} - J_2 \sum_{(pq)} \mathbf{S}_p \cdot \mathbf{S}_q \quad (3)$$

where \mathbf{S}_p and \mathbf{S}_{Cr} are the spin angular momentum operators for the p^{th} dysprosium ion and the chromium ion, respectively, with J_1 and J_2 denoting the appropriate exchange coupling constants for Dy-Cr and Dy-Dy interactions. To account for intramolecular magnetic dipole interactions, we implement the well known magnetic dipole-dipole interaction Hamiltonian

$$H_{\text{dip}} = \frac{\mu_0}{4\pi} \sum_{pq} \left[\frac{\mathbf{M}_p \cdot \mathbf{M}_q}{|\mathbf{R}_{pq}|^3} - 3 \frac{(\mathbf{M}_p \cdot \mathbf{R}_{pq})(\mathbf{M}_q \cdot \mathbf{R}_{pq})}{|\mathbf{R}_{pq}|^5} \right] \quad (4)$$

where μ_0 is the vacuum permeability, \mathbf{M}_p is the magnetic moment of the p^{th} ion, \mathbf{R}_{pq} is a vector connecting the ions p and q and the sum ranges over all Dy^{III} and Cr^{III} ions.

The zero-field splitting of Cr^{III} is well described by the Hamiltonian

$$H_{\text{zfs}} = -D(\mathbf{S}_{\text{Cr}} \cdot \mathbf{e}_z)^2 + E \left((\mathbf{S}_{\text{Cr}} \cdot \mathbf{e}_x)^2 - (\mathbf{S}_{\text{Cr}} \cdot \mathbf{e}_y)^2 \right) \quad (5)$$

where \mathbf{e}_i , $i \in \{x, y, z\}$ are unit vectors specifying the ab initio determined magnetic anisotropy axes of the ion and $D = 0.25 \text{ cm}^{-1}$ and $E = 8 \times 10^{-3} \text{ cm}^{-1}$ are the axial and rhombic zero-field splitting parameters, respectively, also taken from the ab initio calculations. Finally, the Zeeman Hamiltonian reads

$$H_{\text{Zee}} = \mathbf{B} \cdot \left(g\mu_B \mathbf{S}_{\text{Cr}} + \sum_{p=1}^3 \mathbf{M}_p \right) \quad (6)$$

where $\mathbf{B} = (\cos(\phi_F) \cos(\eta_F), \sin(\phi_F) \cos(\eta_F), \sin(\eta_F))$ and η_F, ϕ_F define the orientation of the applied magnetic field.

We account for a coupling between the magnetic subsystem, lattice vibrations and stray fields causing Dy^{III} spin flips via the Redfield master equation for the reduced density matrix populations^{37,39}

$$\dot{\rho}_m = \sum_k (W^{k \rightarrow m}(t) + \Omega^{k \leftrightarrow m}(t)) \rho_k - \rho_m \sum_k (W^{m \rightarrow k}(t) + \Omega^{m \leftrightarrow k}(t)) \quad (7)$$

expressed on the instantaneous energy eigenbasis of Eq. (2). The time-evolution of ρ_m is determined both by $W^{k \rightarrow m}(t)$ and $\Omega^{k \leftrightarrow m}(t)$ which account for spin-lattice mediated magnetic relaxation and stray-field assisted quantum tunnelling of the magnetisation from state k to state m owing to spin flips of the Dy^{III} magnetic moments. A detailed explanation of these rates and their derivations can be found in ref. 37. Upon numerical integration of Eq. (7), we calculate the single-crystal magnetisation as

$$M = \text{Tr} \left\{ \hat{\mathbf{n}} \cdot \left(g\mu_B \mathbf{S}_{\text{Cr}} + \sum_{p=1}^3 \mathbf{M}_p \right) \rho \right\} \quad (8)$$

where $\hat{\mathbf{n}}$ is a normal vector along the direction of the applied magnetic field.

To simulate the powder EPR spectrum of MDy₆ we employ the Fermi golden rule to calculate radiation-induced transitions between magnetic states $|i\rangle$ and $|f\rangle$ according to

$$I^{i \rightarrow f} = \frac{I_0}{\pi} \frac{\Gamma}{(\omega_f - \nu)^2 + \Gamma^2} |\langle f | \mathbf{M} \cdot \mathbf{e}_\perp | i \rangle|^2 (P_i - P_f) \quad (9)$$

where $|i\rangle$ and $|f\rangle$, like the energy spacing $\omega_f = (E_f - E_i)/\hbar$, implicitly depend upon $|\mathbf{B}|$ as well as on the relative orientation of the molecule to the applied magnetic field. P_f and P_i are the Boltzmann populations of states i and f , \mathbf{M} is the total magnetic moment of the polynuclear cluster and \mathbf{e}_\perp is a normal vector specifying the direction of radiation propagation, taken here to be perpendicular to the applied field in the lab frame. For a given direction and magnitude of the applied field, Eq. (9) is summed over for all initial and final states $|i\rangle$ and $|f\rangle$. For the powder averaging, the total signal $I = \sum_{fi} I^{i \rightarrow f}$ is averaged over the unit sphere using Lebedev quadrature.

Data availability

The X-ray crystallographic coordinates for the structure reported in this study have been deposited at the Cambridge Crystallographic Data Centre (CCDC), under deposition number 2106845. These data can be obtained free of charge from the Cambridge Crystallographic Data Centre via www.ccdc.cam.ac.uk/data_request/cif.

Code availability

The Mathematica notebooks used for the implementation of the theoretical models of spin dynamics and electron paramagnetic resonance are available from the corresponding authors upon reasonable request.

Received: 7 April 2022; Accepted: 22 November 2024; Published online: 24 December 2024

References

1. Tang, J. et al. Dysprosium triangles showing single-molecule magnet behavior of thermally excited spin states. *Angew. Chem. Int. Ed.* **118**, 1761 (2006).
2. Luzon, J. et al. Spin chirality in a molecular dysprosium triangle: the archetype of the noncollinear Ising model. *Phys. Rev. Lett.* **100**, 247205 (2008).
3. Soncini, A. & Chibotaru, L. F. Toroidal magnetic states in molecular wheels: Interplay between isotropic exchange interactions and local magnetic anisotropy. *Phys. Rev. B* **77**, 220406 (2008).
4. Chibotaru, L. F., Ungur, L. & Soncini, A. The origin of nonmagnetic kramers doublets in the ground state of dysprosium triangles: evidence for a toroidal magnetic moment. *Angew. Chem.* **120**, 4194 (2008).
5. Murray, K. S. *Single Molecule Toroids: Synthetic Strategies, Theory and Applications* (Springer International Publishing, 2022).
6. Zvezdin, A. K., Kostyuchenko, V. V., Popov, A. I., Popkov, A. F. & Ceulemans, A. Toroidal moment in the molecular magnet V_{15} . *Phys. Rev. B* **80**, 172404 (2009).
7. Popov, A., Plokhov, D. & Zvezdin, A. Anapole moment and spin-electric interactions in rare-earth nanoclusters. *EPL* **87**, 67004 (2009).
8. Plokhov, D. I., Zvezdin, A. K. & Popov, A. I. Macroscopic quantum dynamics of toroidal moment in Ising-type rare-earth clusters. *Phys. Rev. B* **83**, 184415 (2011).
9. Plokhov, D. I., Popov, A. I. & Zvezdin, A. K. Quantum magnetoelectric effect in the molecular crystal Dy. *Phys. Rev. B* **84**, 224436 (2011).
10. Ungur, L., Lin, S.-Y., Tang, J. & Chibotaru, L. F. Single-molecule toroids in Ising-type lanthanide molecular clusters. *Chem. Soc. Rev.* **43**, 6894 (2014).
11. Popov, A., Plokhov, D. & Zvezdin, A. Magnetolectricity of single molecular toroids: The Dy_4 ring cluster. *Phys. Rev. B* **94**, 184408 (2016).
12. Guo, P.-H. et al. The first Dy_4 single-molecule magnet with a toroidal magnetic moment in the ground state. *Inorg. Chem.* **51**, 1233 (2012).
13. Das, C. et al. Single-molecule magnetism, enhanced magnetocaloric effect, and toroidal magnetic moments in a family of Ln_4 squares. *Chem. Eur. J.* **21**, 15639 (2015).
14. Fernandez Garcia, G. et al. A Dy_4 cubane: a new member in the single-molecule toroids family. *Angew. Chem. Int. Ed.* **130**, 17335 (2018).
15. Trif, M., Troiani, F., Stepanenko, D. & Loss, D. Spin-electric coupling in molecular magnets. *Phys. Rev. Lett.* **101**, 217201 (2008).
16. Georgeot, B. & Mila, F. Chirality of triangular antiferromagnetic clusters as a qubit. *Phys. Rev. Lett.* **104**, 200502 (2010).
17. Soncini, A. & Chibotaru, L. F. Molecular spintronics using noncollinear magnetic molecules. *Phys. Rev. B* **81**, 132403 (2010).
18. Crabtree, J. M. & Soncini, A. Toroidal quantum states in molecular spin-frustrated triangular nanomagnets with weak spin-orbit coupling: applications to molecular spintronics. *Phys. Rev. B* **98**, 094417 (2018).
19. Rao, S., Ashtree, J. & Soncini, A. Toroidal moment in a family of spin-frustrated heterometallic triangular nanomagnets without spin-orbit coupling: applications in a molecular spintronics device. *Physica B Condens. Matter* **592**, 412237 (2020).
20. Pavlyukh, Y. Toroidal spin states in molecular magnets. *Phys. Rev. B* **101**, 144408 (2020).
21. Faglioni, F., Ligabue, A., Pelloni, S., Soncini, A. & Lazzaretti, P. Molecular response to a time-independent non-uniform magnetic-field. *Chem. Phys.* **304**, 289 (2004).
22. Spaldin, N. A., Fiebig, M. & Mostovoy, M. The toroidal moment in condensed-matter physics and its relation to the magnetoelectric effect. *J. Phys. Condens. Matter* **20**, 434203 (2008).
23. Budker, D. & Romalis, M. Optical magnetometry. *Nat. Phys.* **3**, 227 (2007).
24. Taylor, J. et al. High-sensitivity diamond magnetometer with nanoscale resolution. *Nat. Phys.* **4**, 810 (2008).
25. Kügel, J. et al. Reversible magnetic switching of high-spin molecules on a giant Rashba surface. *npj Quantum Mater.* **3**, 53 (2018).
26. Schirhagl, R., Chang, K., Lorez, M. & Degen, C. L. Nitrogen-vacancy centers in diamond: nanoscale sensors for physics and biology. *Annu. Rev. Phys. Chem.* **65**, 83 (2014).
27. Qiu, Z., Vool, U., Hamo, A. & Yacoby, A. Nuclear spin assisted magnetic field angle sensing. *npj Quantum Inf.* **7**, 1 (2021).
28. Kitching, J., Knappe, S. & Donley, E. A. Atomic sensors—a review. *IEEE Sens. J.* **11**, 1749 (2011).
29. Degen, C. L., Reinhard, F. & Cappellaro, P. Quantum sensing. *Rev. Mod. Phys.* **89**, 035002 (2017).
30. Osterwalder, A. & Merkt, F. Using high Rydberg states as electric field sensors. *Phys. Rev. Lett.* **82**, 1831 (1999).
31. Zadrozny, J. M., Gallagher, A. T., Harris, T. D. & Freedman, D. E. A porous array of clock qubits. *J. Am. Chem. Soc.* **139**, 7089 (2017).
32. Wojnar, M. K., Laorenza, D. W., Schaller, R. D. & Freedman, D. E. Nickel (II) metal complexes as optically addressable qubit candidates. *J. Am. Chem. Soc.* **142**, 14826 (2020).
33. Yu, C., Von Kugelgen, S., Laorenza, D. W. & Freedman, D. E. A molecular approach to quantum sensing. *ACS Cent. Sci.* **7**, 712 (2021).
34. Hewitt, I. J. et al. Coupling Dy_3 triangles enhances their slow magnetic relaxation. *Angew. Chem. Int. Ed.* **49**, 6352 (2010).
35. Novitchi, G. et al. Heterometallic Cu^{II}/Dy^{III} 1D chiral polymers: chirogenesis and exchange coupling of toroidal moments in trinuclear Dy_3 single molecule magnets. *Chem. Sci.* **3**, 1169 (2012).
36. Lin, S.-Y. et al. Coupling Dy_3 triangles to maximize the toroidal moment. *Angew. Chem. Int. Ed.* **51**, 12767 (2012).
37. Vignesh, K. R. et al. Ferrotoroidic ground state in a heterometallic $Cr^{III}Dy_6^{III}$ complex displaying slow magnetic relaxation. *Nat. Commun.* **8**, 1 (2017).
38. Vignesh, K. R. et al. Slow Magnetic Relaxation and Single-Molecule Toroidal Behaviour in a Family of Heptanuclear $Cr^{III}Ln_6^{III}$ ($Ln=Tb, Ho, Er$) Complexes. *Murray. Angew. Chem. Int. Ed.* **130**, 787 (2018).
39. Ashtree, J. M. et al. Tuning the ferrotoroidic coupling and magnetic hysteresis in double-triangle complexes $Dy_3M^{III}Dy_3$ via the M^{III} -linker. *Eur. J. Inorg. Chem.* **2021**, 435 (2021).
40. Zimmermann, A. S., Meier, D. & Fiebig, M. Ferroic nature of magnetic toroidal order. *Nat. Commun.* **5**, 1 (2014).
41. Park, P. et al. Field-tunable toroidal moment and anomalous Hall effect in noncollinear antiferromagnetic Weyl semimetal $Co_{1/3}TaS_2$. *npj Quantum Mater.* **7**, 42 (2022).
42. Park, K. et al. Nonreciprocal directional dichroism at telecom wavelengths. *npj Quantum Mater.* **7**, 38 (2022).
43. Zhang, J. et al. A ferrotoroidic candidate with well-separated spin chains. *Adv. Mater.* **34**, 2106728 (2022).
44. Wernsdorfer, W., Orozco, E. B., Barbara, B., Benoit, A. & Mailly, D. Classical and quantum magnetisation reversal studied in single nanometer-sized particles and clusters using micro-SQUIDS. *Phys. B Condens. Matter* **280**, 264 (2000).
45. Aquilante, F. et al. Molcas 8: new capabilities for multiconfigurational quantum chemical calculations across the periodic table. *J. Comput. Chem.* **37**, 506 (2016).
46. Clark, R. & Reid, J. The analytical calculation of absorption in multifaceted crystals. *Acta Crystallogr. A* **51**, 887 (1995).
47. Sheldrick, G. M. A short history of SHELX. *Acta Crystallogr. A* **64**, 112 (2008).
48. Sheldrick, G. *SHELXL-97, Program for X-ray Crystal Structure Refinement* (Göttingen University, 1997).
49. Hess, B. A., Marian, C. M., Wahlgren, U. & Gropen, O. A mean-field spin-orbit method applicable to correlated wavefunctions. *Chem. Phys. Lett.* **251**, 365 (1996).
50. Roos, B. & Malmqvist, P. Relativistic quantum chemistry: the multiconfigurational approach. *Phys. Chem. Chem. Phys.* **11**, 2919 (2004).

51. Roos, B. et al. New relativistic atomic natural orbital basis sets for lanthanide atoms with applications to the Ce diatom and LuF_3 . *J. Phys. Chem. A* **112**, 11431 (2008).
52. Chibotaru, L. F. & Ungur, L. Ab initio calculation of anisotropic magnetic properties of complexes. I. Unique definition of pseudospin Hamiltonians and their derivation. *J. Chem. Phys.* **137**, 064112 (2012).
53. Gagliardi, L., Lindh, R. & Karlström, G. Local properties of quantum chemical systems: the LoProp approach. *J. Chem. Phys.* **121**, 4494 (2004).
54. Becke, A. D. Becke's three parameter hybrid method using the LYP correlation functional. *J. Chem. Phys.* **98**, 5648 (1993).
55. Frisch, M. J. et al. *Gaussian 09, Rev. A.02* (Gaussian, 2009).

Acknowledgements

A.S. acknowledges financial support via the grant P-DiSC BIRD2023-UNIPD, from the Department of Chemical Sciences of the University of Padova and from the Australian Research Council (Discovery Project no. DP210103208 and FT180100519). A.S. and K.S.M. acknowledge funding from the University of Padova and Monash University Joint Initiative in Research (2024 Seed Fund scheme) for the project Single Molecule Toroids for Quantum Computation. G.R. would like to acknowledge DST/SERB, India, for financial support (CRG/2018/000430, DST/SJF/CSA03/2018-10; SB/SJF/2019-20/12). A.S. acknowledges the CINECA award under the ISCRA initiative, Project Grant SMTQUAN: Single Molecule Toroids for Quantum Computation, for the availability of high-performance computing resources and support. K. H. acknowledges financial support from the Revolutionary Energy Storage Systems Future Science Platform.

Author contributions

K.R.V., S.K.L., D.C., M.S. and K.S.M. synthesised the CrDy_3 molecule and S.L.B and S.K.L. performed X-ray scattering experiments. W.W. performed μ -SQUID measurements. D.C., D.B. and M.S. performed isothermal powder magnetisation and magnetic susceptibility measurements. K.R.V., A. Swain and G.R. performed ab initio calculations, DFT calculations and charge density analysis. K.H. and A. Soncini were responsible for theoretical modelling and writing the paper.

Competing interests

The authors declare no competing interests.

Additional information

Supplementary information The online version contains supplementary material available at <https://doi.org/10.1038/s41535-024-00712-9>.

Correspondence and requests for materials should be addressed to Kieran Hymas, Alessandro Soncini, Gopalan Rajaraman, Stuart K. Langley or Keith S. Murray.

Reprints and permissions information is available at <http://www.nature.com/reprints>

Publisher's note Springer Nature remains neutral with regard to jurisdictional claims in published maps and institutional affiliations.

Open Access This article is licensed under a Creative Commons Attribution-NonCommercial-NoDerivatives 4.0 International License, which permits any non-commercial use, sharing, distribution and reproduction in any medium or format, as long as you give appropriate credit to the original author(s) and the source, provide a link to the Creative Commons licence, and indicate if you modified the licensed material. You do not have permission under this licence to share adapted material derived from this article or parts of it. The images or other third party material in this article are included in the article's Creative Commons licence, unless indicated otherwise in a credit line to the material. If material is not included in the article's Creative Commons licence and your intended use is not permitted by statutory regulation or exceeds the permitted use, you will need to obtain permission directly from the copyright holder. To view a copy of this licence, visit <http://creativecommons.org/licenses/by-nc-nd/4.0/>.

© The Author(s) 2024